Evaluation of Electromagnetic Scattering by Conducting Bodies of Revolution With Discontinuous Currents

Úrsula C. Resende[1], Fernando J. S. Moreira[2], José R. Bergmann[3], and Sandro T. M. Gonçalves[1]

[1]Federal Center for Technological Education of Minas Gerais, Belo Horizonte MG 35510-000, Brazil
[2]Federal University of Minas Gerais, Belo Horizonte MG 31270-901, Brazil
[3]Catholic University of Rio de Janeiro, Rio de Janeiro RJ 22453-900, Brazil

In this paper, the electromagnetic scattering by conducting bodies of revolution with discontinuities in the equivalent surface currents is investigated. The simulations are based on the combined field integral equation evaluated by the method of moments. A strategy for implementing an integral equation formulation with appropriate testing functions is presented. The procedure is applied in the analysis of the TE_{11} mode propagation inside a circular waveguide and the radiation from a circular corrugated horn antenna. The effectiveness of the proposed method is illustrated by comparing numerical results with analytical and experimental data.

***Index Terms*—Electric and magnetic field integral equations, electromagnetic scattering by bodies of revolution (BORs), Galerkin method (GM), horn antenna, method of moments (MoM).**

I. Introduction

PROBLEMS involving the electromagnetic scattering from conducting and dielectric bodies have been a subject of intense investigations. Research efforts have led to the development of several analysis tools and modeling techniques [1]–[3]. Surface integral equations evaluated by the method of moments (MoM) are among the most widely used and suitable ones for numerical simulations [4], [5]. When dealing with closed conducting bodies, the combined field integral equation (CFIE) is largely employed due to its capacity to reduce spurious numerical resonances [6].

Although CFIE has been extensively used in the analysis of arbitrary composite bodies, with intricate junctions between different materials [7]–[9], few studies have investigated its application in problems with discontinuous equivalent currents [10], [11], particularly for bodies of revolution (BORs). Electric or magnetic current discontinuities require the use of numerical models to embody those discontinuities. However, such models usually lead to numerical restrictions in the solution [10]. To address such fact, in this paper, the CFIE is solved by a MoM approach slightly different from the Galerkin method (GM). Basis functions that incorporate current discontinuities are adopted and the weighting process is strengthened by the use of local test functions over the complete scatter surface.

To illustrate the usefulness of the proposed technique, the TE_{11} mode propagation inside a circular waveguide and the radiation from a circular corrugated horn are investigated. Numerical simulations of the TE_{11} mode propagation in a circular waveguide are compared with analytical results to validate the proposed approach (PA). Furthermore, simulations of a corrugated horn radiation are compared with measured data and simulations obtained from commercial software to illustrate the influence of the PA in the electromagnetic analysis of the horn's radiation.

Manuscript received June 24, 2015; revised September 15, 2015; accepted September 29, 2015. Date of publication October 7, 2015; date of current version February 17, 2016. Corresponding author: Ú. C. Resende (e-mail: resendeursula@des.cefetmg.br).

Digital Object Identifier 10.1109/TMAG.2015.2487869

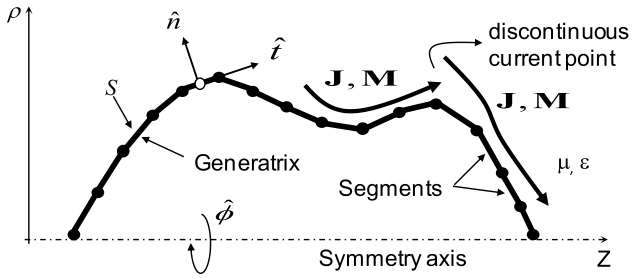

Fig. 1. Generatrix of a BOR.

II. Integral Equation and MoM Solution

Considering the BOR shown in Fig. 1, just over the surface (S) of the object, the CFIE is represented by the linear combination $\alpha\text{TE} + \beta\text{NH}$

$$\begin{aligned}\text{TE} \rightarrow\ & 2\int_S \mathbf{W}(\boldsymbol{r})\cdot(\eta\mathbf{L}(\mathbf{J})+\mathbf{K}(\mathbf{M})+\mathbf{E}^i)ds \\ =\ & -\int_S \mathbf{W}(\boldsymbol{r})\cdot(\hat{\boldsymbol{n}}\times\mathbf{M})ds \qquad (1)\\ \text{NH} \rightarrow\ & 2\int_S \mathbf{W}(\boldsymbol{r})\cdot\hat{\boldsymbol{n}}\times\left(\mathbf{L}(\mathbf{M})/\eta-\mathbf{K}(\mathbf{J})+\mathbf{H}_0^i\right)ds \\ =\ & \int_S \mathbf{W}(\boldsymbol{r})\cdot\mathbf{J}ds \qquad (2)\\ \mathbf{L}(\mathbf{X}) =\ & j/(4\pi k)\int_{S'}[k^2\mathbf{X}(\mathbf{r}')G(\mathbf{r},\mathbf{r}') \\ & -\nabla'\mathbf{X}(\mathbf{r}')\nabla'G(\mathbf{r},\mathbf{r}')]ds' \qquad (3)\\ \mathbf{K}(\mathbf{X}) =\ & -\hat{\boldsymbol{n}}\times\mathbf{X}(\mathbf{r})/2+1/(4\pi)\int_{S'}[\mathbf{X}(\mathbf{r}')\times\nabla'G(\mathbf{r},\mathbf{r}')]ds' \qquad (4)\end{aligned}$$

where α and β are the scalar weights, $\hat{\boldsymbol{n}}$ is the unit outward normal vector to S, $\mathbf{W}$ is the test function, $\mathbf{X}$ is either the equivalent electric ($\mathbf{J}$) or the magnetic ($\mathbf{M}$) surface current, $\mathbf{E}^i$ and $\mathbf{H}^i$ are the electric and magnetic incident fields

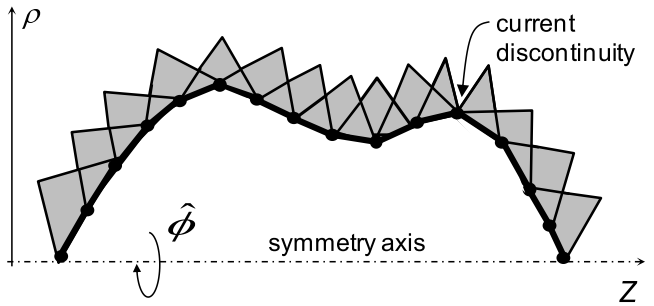

Fig. 2. BOR: triangular functions distribution.

radiated by external sources, respectively, k and η are the wavelength number and intrinsic impedance of the medium, respectively, and $G(\mathbf{r}, \mathbf{r}')$ is the free-space Green's function.

In the numerical solution of the CFIE by the MoM with GM, the basis functions used to represent **J** and **M** are identical to the weight (test) functions. However, for BORs (as the one shown in Fig. 1), the normal term of the CFIE [NH in (2), where a cross product by $\hat{n}$ is present] contains a reciprocal interchange between the test functions in $\hat{t}$- and $\hat{\phi}$-directions. Furthermore, if the $\hat{t}$- and $\hat{\phi}$-components of **J** or **M** have different local behaviors (e.g., discontinuities), the numbers of basis functions used to represent these $\hat{t}$- and $\hat{\phi}$-components will probably be different from each other. Consequently, in the Galerkin approach, each TE and NH terms of the CFIE will be tested by a different number of test functions to provide the MoM linear system of equations. This leads to difficulties in the numerical implementation of the CFIE, which are enhanced by the fact that the integrand of **K** presents more severe singularities than the one of **L** [12], [13].

In this paper, the surface equivalent currents **J** and **M** are expanded by triangular basis functions (TBF), T_j, as

$$\mathbf{J} = \sum_{j=1}^{N} (T_j(\mathbf{r}')/\rho') I_j^J \text{ and } \mathbf{M} = \sum_{j=1}^{N} (T_j(\mathbf{r}')/\rho') I_j^M \quad (5)$$

where N is the number of TBFs and I_j^J and I_j^M are the unknown electric and magnetic current coefficients, respectively. In the present technique, for segments where **J** and **M** are continuous, the TBFs are represented by complete triangles, each one defined over two consecutive segments. At points, where **J** or **M** is discontinuous, half triangles are adopted at the adjacent segments, as shown in Fig. 2.

For the MoM solution of the scattering/radiation problem using the conventional GM, the test functions should be defined as the TBFs, i.e., using half or complete triangles for discontinuous or continuous surface currents, respectively. However, it will be shown here that the best strategy is to always adopt complete triangular test functions (TTF). In any event, all integrals appearing in the calculation of the MoM full-matrix elements are evaluated by Gaussian quadratures with appropriate treatment to extract integrand singularities whenever present [12], [13].

III. Allocation of TBFs and TTFs

To illustrate the allocation of TBFs and TTFs, where a current discontinuity is present, the circular corrugated horn shown in Fig. 3 is considered [4]. Inside the circular waveguide of the horn, at its end-wall ($z = 0.08\lambda$, where $\lambda = 1$ m is the free-space wavelength at the central frequency f_o), electric ($\mathbf{J}_g$) and magnetic ($\mathbf{M}_g$) surface current sources are imposed to excite the fundamental TE_{11} mode. At the same wall, an impedance boundary condition (IBC) is imposed to work as a perfect absorber for the returned TE_{11} mode [4], as shown in Fig. 4(a). Consequently, at the waveguide end-wall, there are equivalent currents **J** and **M**, related to each other by the IBC.

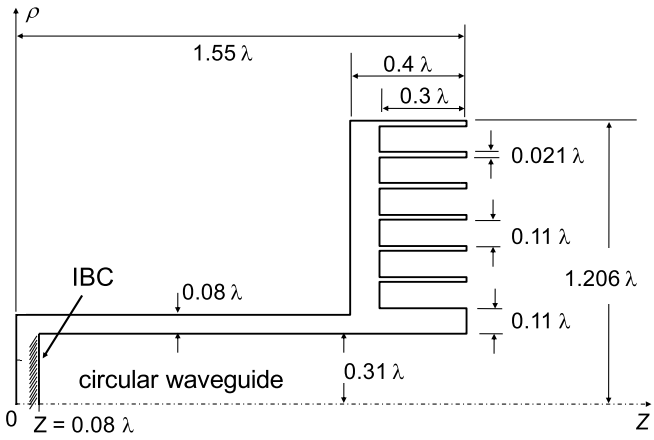

Fig. 3. Circular 90° corrugated horn excited by the fundamental TE_{11} mode.

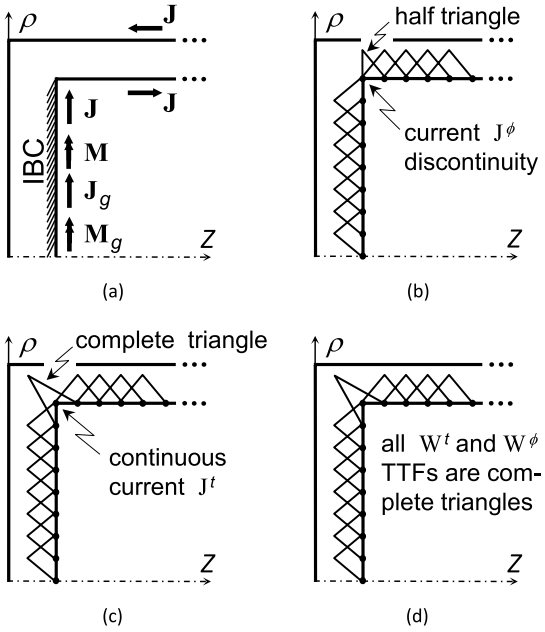

Fig. 4. Horn's circular waveguide end-wall. (a) Equivalent current distributions. (b) Waveguide TBFs for the discontinuous J^ϕ. (c) Waveguide TBFs for the continuous J^t. (d) Waveguide TTFs for W^t and W^ϕ.

The horn shown in Fig. 3 presents a discontinuity in the equivalent surface currents at the internal border of the end-wall ($z = 0.08\lambda$ and $\rho = 0.31\lambda$), where caution should be taken when choosing appropriate TBFs and TTFs. As **M** is related to **J** by the IBC, their TBFs are of no concern in the following discussion. The $\hat{\phi}$-component of **J** (J^ϕ) is proportional to the $\hat{\rho}$-component of the TE_{11} magnetic field (H^ρ) at the waveguide end-wall, which is zero for $\rho = 0.31\lambda$.

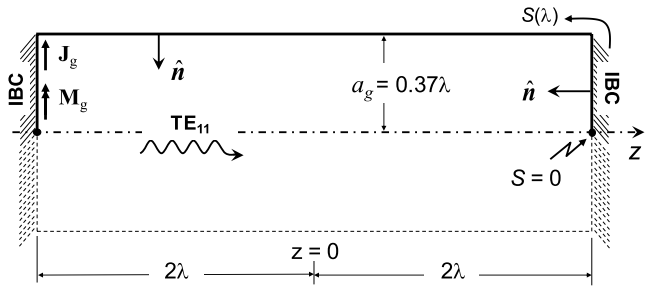

Fig. 5. Circular waveguide excited by the fundamental TE_{11} mode.

However, at the waveguide sidewall, J^{ϕ} is proportional to the z-component of the TE_{11} magnetic field (H^z), which does not vanish. Thus, J^{ϕ} has a discontinuity at the internal border of the waveguide end-wall and a half-triangle should be used, as shown in Fig. 4(b). Similar reasoning can be adopted to show that the $\hat{t}$-component of $\mathbf{J}$ (J^t) is continuous and its TBFs are chosen to be complete triangles, as shown in Fig. 4(c).

If GM is adopted, the $\hat{t}$- and $\hat{\phi}$-components of $\mathbf{W}$ (W^t and W^{ϕ}, respectively) should be specified as done for J^t and J^{ϕ}, however, that would imply in a poorly tested region over the waveguide end-wall close to its border [see Fig. 4(b)]. Instead, complete-triangle TTFs should be used to represent all the W^t and W^{ϕ} components, as shown in Fig. 4(d). Doing so, the boundary conditions are appropriately imposed at both sides of the discontinuity. In Section IV, numerical results will demonstrate that this choice of TTFs, hereinafter, called PA is more appropriate than the GM when the equivalent currents present local discontinuities.

IV. Numerical Results

To demonstrate the effectiveness of the proposed strategy, the circular waveguide shown in Fig. 5 was analyzed. Its radius $a_g = 0.37\lambda$ is set to only allow the propagation of the fundamental TE_{11} mode. At the end-wall $z = -2\lambda$, source currents $\mathbf{J}_g$ and $\mathbf{M}_g$ are imposed to excite the TE_{11} mode propagating in the positive z-direction. At both $z = \pm 2\lambda$ walls, IBCs are placed to work as perfect absorbers for the TE_{11} mode [4]. Consequently, the present model simulates an infinite circular waveguide for $z > 0$. A total of 190 segments were used to represent the waveguide generatrix $S(\lambda)$, for $0 \leq S \leq 4.74\lambda$. At the borders of both end-walls ($\rho = 0.37\lambda$ and $z = \pm 2\lambda$), the TBFs and TTFs allocations were carried on as discussed in Section III, being the PA compared against the traditional GM. Fig. 6 shows the computed surface electric current $\mathbf{J}$ (amplitude and phase for both the $\hat{t}$- and $\hat{\phi}$-components) as a function of $S(\lambda)$. The results obtained from the PA and GM approaches are compared with analytical ones ($\mathbf{J}_{TE11} = \boldsymbol{n} \times \mathbf{H}_{TE11}$) [14]. In general, from Fig. 6, one observes that the PA results present an excellent agreement with the analytical solutions, while the GM results present significant discrepancies. For instance, from Fig. 6(a) and (c), one observes that when PA is used, $|\mathbf{J}| \approx 0$ at $z = -2\lambda$ ($S > 4.37\lambda$) as expected, for no returned TE_{11} mode should be generated, however, that does not happen when GM is adopted. It is interesting to observe in Fig. 6(c) the discontinuity of $|J^{\phi}|$

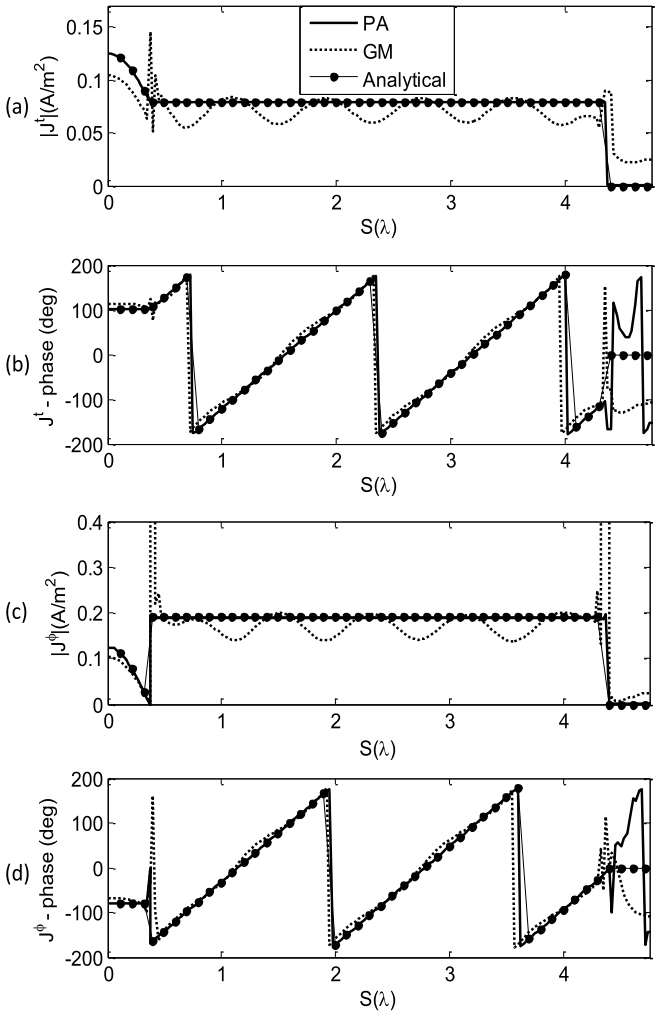

Fig. 6. Electric surface current $\mathbf{J}$ along the waveguide generatrix $S(\lambda)$. (a) J^t amplitude. (b) J^t phase. (c) J^{ϕ} amplitude. (d) J^{ϕ} phase. PA (solid lines) and GM (dashed lines) results compared against analytical solutions [14].

at the border of the waveguide end-wall ($S = 0.37\lambda$), while $|J^t|$ is continuous [Fig. 6(a)]. Furthermore, one observes, from Fig. 6(b) and (d), that the PA predicts a progressive phase distribution along the waveguide and a uniform phase distribution at $z = 2\lambda$ ($S < 0.37\lambda$), as expected. Excluding the domain $4.37\lambda \leq S \leq 4.74\lambda$, where phase numerical errors are present due to the negligible amplitude of $\mathbf{J}$ ($|\mathbf{J}| \approx 0$), in Fig. 6(b), the maximum phase differences between numerical and analytical results are 0.34° for PA and 29.71° for GM, while in Fig. 6(d), the maximum phase differences are 0.33° for PA and 64.09° for GM.

In the second numerical study, the radiation pattern of the circular corrugated horn shown in Fig. 3 was simulated. A total of 471 segments were used to represent the horn's generatrix in the PA and GM analyses. The E- and H-plane radiation patterns of the horn at the central frequency f_o ($\lambda = 1$ m) are shown in Fig. 7, where the PA and GM numerical results are compared with measured data [4] and numerical simulations obtained by the software Computer Simulation Technology (CST). It is clear from Fig. 7 that the results of

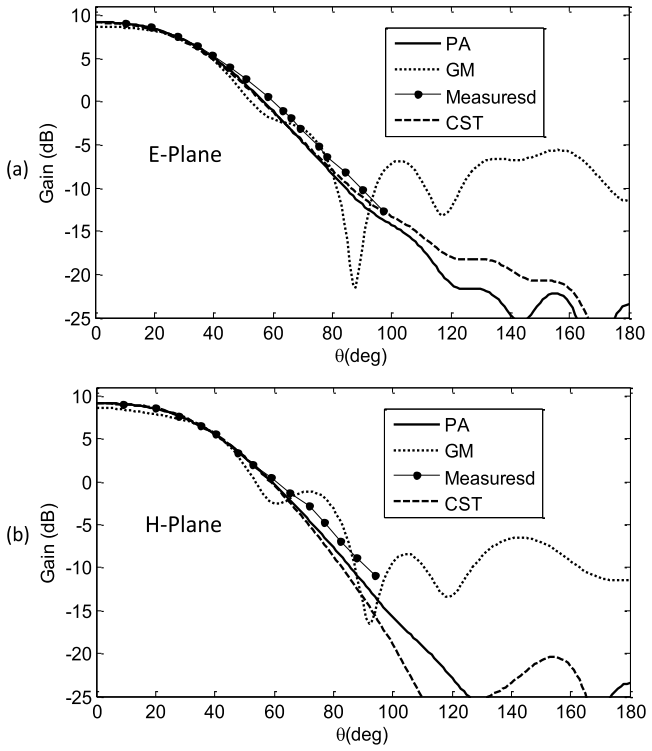

Fig. 7. Radiation pattern of the corrugated horn. (a) E-plane. (b) H-plane.

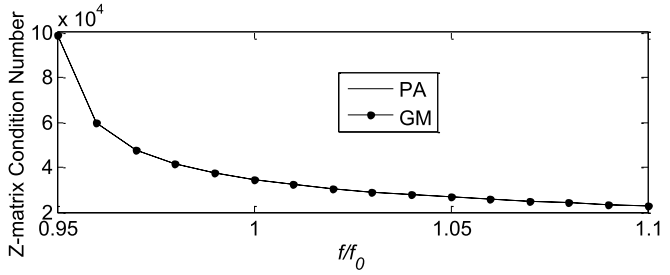

Fig. 8. MoM Z-matrix condition number of the corrugated horn analyses.

the PA are in better agreement with the measured data and CST simulations than the GM results, particularly far away from the horn's bore-sight ($\theta > 50°$). In Fig. 8, the MoM Z-matrix condition number for both PA and GM is shown along the frequency range $0.95 f_o < f < 1.1 f_o$. Although the PA provides a nonsymmetrical MoM Z-matrix, its condition number is not significantly altered with respect to that of the GM in the horn's analysis. Its value decreases with frequency, as one can observe from Fig. 8. This is an expected result as the Z-matrix changes associated with the PA are marginal.

V. Conclusion

An approach to overcome difficulties aroused by surface current discontinuities in the numerical implementation of the MoM-CFIE was proposed. The strategy is grounded on not using GM at places where current discontinuities are present. Comparisons with analytical solutions and measured data show that the technique successfully simulates the TE_{11} mode propagation inside a circular waveguide and the radiation from a circular corrugated horn antenna.

Acknowledgment

This work was supported in part by the Fundação de Amparo à Pesquisa do Estado de Minas Gerais, in part by the Coordenação de Aperfeiçoamento de Pessoal de Nível Superior, in part by the Conselho Nacional de Desenvolvimento Científico e Tecnológico, and in part by the Centro Federal de Educação Tecnológica de Minas Gerais.

References

[1] J.-V. Rodríguez, F. Quesada-Pereira, L. Juan-Llácer, J.-M. Molina-Garcia-Pardo, and A. Álvarez-Melcón, "UTD-PO radiation pattern analysis of rectangular horn antennas with cylindrical corrugations," *IEEE Trans. Antennas Propag.*, vol. 62, no. 11, pp. 5911–5915, Nov. 2014.

[2] M. A. Elmansouri and D. S. Filipovic, "Reduced-size TEM horn for short-pulse high-power electromagnetic systems," in *Proc. IEEE Antennas Propag. Soc. Int. Symp. (APSURSI)*, Jul. 2014, pp. 828–829.

[3] R. Jana and R. Bhattacharjee, "Analysis of scattering parameters of a stepped cylindrical horn containing inner posts using MM and 2-D FEM," in *Proc. IEEE 20th Nat. Conf. Commun. (NCC)*, Feb./Mar. 2014, pp. 1–6.

[4] K. A. Iskander, L. Shafai, A. Frandsen, and J. E. Hansen, "Application of impedance boundary conditions to numerical solution of corrugated circular horns," *IEEE Trans. Antennas Propag.*, vol. 30, no. 3, pp. 366–372, May 1982.

[5] Z. Peng and J.-F. Lee, "Advanced integral equation solvers for high-fidelity electromagnetic modeling and simulation," in *Proc. Int. Conf. IEEE Electromagn. Adv. Appl. (ICEAA)*, Aug. 2014, pp. 272–275.

[6] J. R. Mautz and R. F. Harrington, "H-field, E-field, and combined-field solutions for conducting bodies of revolution," *Int. J. Electron. Commun.*, vol. 32, no. 4, pp. 157–164, 1978.

[7] Ú. C. Resende, F. J. S. Moreira, and O. M. C. Pereira-Filho, "EMFIE and MEFIE formulations for the analysis of scattering from dielectric and composite bodies of revolution," *Microw. Opt. Technol. Lett.*, vol. 53, no. 2, pp. 398–402, Feb. 2011.

[8] X. Q. Sheng, J.-M. Jin, J. Song, W. C. Chew, and C.-C. Lu, "Solution of combined-field integral equation using multilevel fast multipole algorithm for scattering by homogeneous bodies," *IEEE Trans. Antennas Propag.*, vol. 49, no. 11, pp. 1718–1726, Nov. 2001.

[9] J. M. Putnam and L. N. Medgyesi-Mitschang, "Combined field integral equation formulation for inhomogeneous two and three-dimensional bodies: The junction problem," *IEEE Trans. Antennas Propag.*, vol. 39, no. 5, pp. 667–672, May 1991.

[10] E. Ubeda, J. M. Rius, and A. Heldring, "Nonconforming discretization of the electric-field integral equation for closed perfectly conducting objects," *IEEE Trans. Antennas Propag.*, vol. 62, no. 8, pp. 4171–4186, Aug. 2014.

[11] M. Jiang, J. Hu, R. Zhao, and Z. Nie, "Surface integral equation based discontinuous Galerkin method for impedance surface objects," in *Proc. IEEE Int. Conf. Comput. Electromagn. (ICCEM)*, Feb. 2015, pp. 175–177.

[12] Ú. C. Resende, F. J. S. Moreira, and O. M. C. Pereira-Filho, "Numerical study of singularity extraction in MoM integrals for scattering from bodies of revolution," *Microw. Opt. Technol. Lett.*, vol. 54, no. 11, pp. 2543–2548, Nov. 2012.

[13] L. Gurel and O. Ergul, "Singularity of the magnetic-field integral equation and its extraction," *IEEE Antennas Wireless Propag. Lett.*, vol. 4, no. 1, pp. 229–232, Aug. 2005.

[14] R. F. Harrington, *Time-Harmonic Electromagnetic Fields*. New York, NY, USA: McGraw-Hill, 1961.